

XMM-Newton and *Chandra* Observations of the Ejecta-Dominated Mixed-Morphology Galactic Supernova Remnant G352.7-0.1

Thomas G. Pannuti¹, Oleg Kargaltsev², Jared P. Napier¹ and Derek Brehm²

ABSTRACT

We present a spatial and spectral X-ray analysis of the Galactic supernova remnant (SNR) G352.7-0.1 using archival data from observations made with the *XMM-Newton* X-ray Observatory and the *Chandra* X-ray Observatory. Prior X-ray observations of this SNR had revealed a thermal center-filled morphology which contrasts with a shell-like radio morphology, thus establishing G352.7-0.1 as a member of the class of Galactic SNRs known as mixed-morphology SNRs (MMSNR). Our study confirms that the X-ray emission comes from the SNR interior and must be ejecta-dominated. Spectra obtained with *XMM-Newton* may be fit satisfactorily with a single thermal component (namely a non-equilibrium ionization component with enhanced abundances of silicon and sulfur). In contrast, spectra extracted by *Chandra* from certain regions of the SNR cannot always be fit by a single thermal component. For those regions, a second thermal component with solar abundances or two thermal components with different temperatures and thawed silicon and sulfur abundances (respectively) can generate a statistically-acceptable fit. We argue that the former scenario is more physically-plausible: based on parameters of our spectral fits, we calculate physical parameters including X-ray-emitting mass ($\sim 45 M_{\odot}$, for solar abundances). We find no evidence for overionization in the X-ray emitting plasma associated with the SNR: this phenomenon has been seen in other MMSNRs. We have conducted a search for a neutron star within the SNR using a hard (2-10 keV) *Chandra* image but could not identify a firm candidate. We also present (for the first time) the detection of infrared emission from this SNR as detected at 24 μm by MIPS aboard *Spitzer*. Finally, we discuss the properties of G352.7-0.1 in the context of other ejecta-dominated MMSNRs.

Subject headings: ISM: individual objects (SNR G352.7-0.1) – ISM : supernova remnants – X-rays: ISM

1. Introduction

The term “supernova remnant” (SNR) refers to the expanding shell of material produced by a supernova explosion: SNRs are typically composed of stellar ejecta mixed with swept-up interstellar material (the latter component tends to dominate over the former component as the SNR ages). SNRs are intimately involved with many processes associated with the interstellar medium

(ISM), such as chemical evolution (through the enrichment of heavy element content) and cosmic-ray acceleration. SNRs have also been detected over a remarkably broad portion of the electromagnetic spectrum ranging from low-energy radio emission (synchrotron radiation) to TeV γ -rays. The observed high-energy emission can come from the SNR shell (forward shock) which accelerates particles to very high energies and the SNR interior (filled with heated ejecta and/or swept-up material and accelerated electrons). In some cases both components are clearly present (composite type SNRs) while in the others only the shell or only the interior emission (center-filled SNRs) could be identified. To date, approximately 280 SNRs are known to exist in our galaxy (Green

¹Space Science Center, Department of Earth and Space Sciences, 235 Martindale Drive, Morehead State University, Morehead, KY 40351; t.pannuti@moreheadstate.edu, jpnapi@moreheadstate.edu

²Department of Physics, 308 Samson Hall, George Washington University, Washington, DC 20052; kargaltsev@gwu.edu, brehm.derek@gmail.com

2009a,b): these sources have been detected chiefly by their radio emission. Based on their radio morphologies, about 78% belong to the shell type, 12% are composite type and 4% are the center-filled type. The remaining 6% are difficult to attribute to any of the above types (Green 2009a,b).

While theories about the evolution of SNRs generally predict that these sources should have shell-like morphologies in the X-ray and radio, a particular class of SNRs known as mixed-morphology SNRs (MMSNRs) have garnered considerable interest from observational, theoretical and computer modeling perspectives (Rho & Petre 1998). These sources feature the nominal shell-like radio morphology typical of SNRs coupled with a thermal center-filled X-ray morphology which is centrally-brightened and roughly homogeneous (Vink 2012). MMSNRs also appear to be associated with molecular clouds, as evidenced by hydroxyl (OH) masers at 1720 MHz that are indicators of interactions between SNR shocks and molecular clouds and by infrared observations that reveal emission associated with shocked molecules. The origin of the contrasting X-ray and radio morphologies that characterize MMSNRs remains a mystery. Several competing theories have been proposed to account for the unusual morphologies exhibited by MMSNRs: one theory is the evaporating cloud theory (White & Long 1991) which states that the interior of an MMSNR is filled with clouds that have survived passage by the initial SNR blast wave. These clouds have thus loaded the interior of the SNR with a reservoir of material and produce thermal X-ray emission as they evaporate. A second theory proposed by Cox et al. (1999) suggests that the overfed thermal emission may be explained by efficient thermal conduction processes within the SNR interior. Unfortunately, neither of these theories can by themselves provide an adequate explanation for the observed X-ray morphology of these particular SNRs. For example, Shelton et al. (2004) noted that both the evaporating cloud model and the thermal conduction model fail to adequately predict the sharp X-ray surface brightness gradient observed for several MMSNRs. A pivotal clue about this phenomenon may rest with the fact that MMSNRs all preferentially appear to be interacting with adjacent molecular clouds. Remarkably, several MMSNRs appear to feature

X-ray-emitting plasma that is dominated by ejecta rather than swept-up material as expected for sources with ages estimated to be $\sim 10^4$ yr (the typical estimated age of an MMSNR). To better understand the X-ray properties of MMSNRs – and specifically MMSNRs with ejecta-dominated X-ray emission – we present an analysis of X-ray observations of the Galactic ejecta-dominated MMSNR G352.7–0.1.

G352.7–0.1 was first classified as a SNR based on observations made at 408 and 5000 MHz of the source by Clark et al. (1973) and Clark et al. (1975) using the Molonglo Cross Radio Observatory and the Parkes 64 Meter Radio Telescope, respectively. Subsequent radio observations of G352.7–0.1 (Caswell et al. 1983; Dubner et al. 1993; Whiteoak & Green 1996; Giacani et al. 2009) with such observatories as the Fleurs Synthesis Telescope, the Very Large Array (VLA) and the Molonglo Observatory Synthesis Telescope at frequencies of 843 MHz and 1400 MHz have revealed a shell-like morphology of this source that features two loops or lobes: the second lobe is an incomplete shell seen toward the southwest of the complete first lobe. The entire angular extent of the SNR is approximately 8×6 arcminutes (Green 2009a) and the integrated spectral index of the SNR is $\alpha \sim -0.6$ (Dubner et al. 1993) (where we have adopted the convention for radio flux densities $S \propto \nu^\alpha$). The assumed distances to G352.7–0.1 have ranged from 7.5 ± 0.5 kpc (Giacani et al. 2009) to 8.5 kpc (Kinugasa et al. 1998) to 11 kpc (Dubner et al. 1993) to 16.4 kpc (Caswell et al. 1983). Based on observations that traced the HI absorption profile in the direction of G352.7–0.1 and considering the Galactic tangent point velocity, Giacani et al. (2009) derived bounds of between ~ 6.8 kpc and ~ 8.4 kpc for the distance to the SNR. Those authors concluded that a value of 7.5 ± 0.5 kpc is a satisfactory distance estimate to G352.7–0.1: we adopt this distance to the SNR in the present paper. In Table 1 we present a summary of the general physical properties of G352.7–0.1.

A bright unresolved radio source is seen on the eastern edge of the complete first lobe and Dubner et al. (1993) speculated that this source may be a “compact inhomogeneity in the radio shell” or an unrelated background source seen against the radio shell by a chance alignment. As pointed

out by Giacani et al. (2009), this radio source was resolved into two separate point-like sources by higher angular resolution observations: these two sources have been cataloged as WBH2005 352.775–0.153 and WBH2005 352.772–0.149 in the “New Catalog of Compact 6cm Sources in the Galactic Plane” (White et al. 2005). To further elucidate the properties of these radio sources, Giacani et al. (2009) computed a spectral index of the combined emission from the two sources (because these two sources were unresolved in the 1.4 GHz map those authors presented of G352.7–0.1), of $\alpha \sim -1.1$ to -1.3 . This estimate of α prompted Giacani et al. (2009) to conclude that these two sources comprise clouds of radio-emitting plasma ejecta by a distant active galactic nuclei seen in projection beyond G352.7–0.1 and thus physically unrelated to the SNR. Therefore, we do not consider these radio sources to be associated with G352.7–0.1. We note that Green et al. (1997) and Koralesky et al. (1998) detected OH maser emission at 1720 MHz from G352.7–0.1: such emission is closely associated with interactions between SNRs and molecular clouds. MMSNRs (like G352.7–0.1) appear to be interacting with adjacent molecular clouds and this interaction is suspected to at help explain the origin of the observed contrasting X-ray and radio morphologies of these sources. Additional evidence for an interaction between G352.7–0.1 and adjacent molecular clouds is supplied by Toledo-Roy et al. (2014), who explain the observed radio morphology using a model where the original supernova explosion occurs inside and near a molecular cloud.

X-ray emission from G352.7–0.1 was first detected by Kinugasa et al. (1998) based on observations made with the Advanced Satellite for Cosmology and Astrophysics (*ASCA*) (Tanaka et al. 1994) as part of the *ASCA* Galactic Plane Survey (see Sugizaki et al. (2001), who also reported the detection of X-ray emission from G352.7–0.1). Spectral analysis of this SNR as performed by Kinugasa et al. (1998) using extracted spectra from the Gas Imaging Spectrometers (GISs) and the Solid State Imaging Spectrometers (SISs) aboard *ASCA* (see Burke et al. (1994), Serlemitsos et al. (1995), Makishima et al. (1996) and Ohashi et al. (1996) for more information about the GISs, the SISs and the XRTs) revealed that the X-ray emitting plasma could be best fit with a non-

equilibrium ionization (NEI) model with an ionization timescale $\tau \sim 10^{11} \text{ cm}^{-3} \text{ s}$ (indicating that the plasma is not in ionization equilibrium) and a temperature of $kT \sim 2 \text{ keV}$ which is unusually high for an SNR. Prominent K-shell lines from highly-ionized silicon, sulfur and argon were also clearly seen in the extracted spectra: the fitted abundances of silicon and sulfur were both overabundant relative to solar abundances (~ 3.7 and ~ 3.4 , respectively) and thus the X-ray-emitting plasma associated with G352.7–0.1 is ejecta-dominated. Lastly, Kinugasa et al. (1998) – who assumed that G352.7–0.1 lies at a distance of 8.5 kpc and that the SNR is in the Sedov stage of evolution – estimated the age of the SNR to be $t \sim 2200 \text{ yr}$. If this age estimate is accurate, then it is remarkable that the X-ray emitting plasma associated with G352.7–0.1 is still ejecta-dominated. We note that a separate spectral analysis of the *ASCA*-detected emission from G352.7–0.1 was conducted by Reynolds & Keohane (1999), who fit the extracted spectra using the synchrotron X-ray emission model SRCUT: this model assumes that all of the observed X-ray continuum emission is produced by synchrotron radiation and is characterized by the radio flux density of the SNR at 1 GHz, the radio spectral index α and the roll-off frequency ν_{rolloff} from which the energy E_{max} (the energy at which the electron energy distribution must steepen from its slope at radio-emitting energies). Based on the results of their fits to the spectra (which were constrained by the observed radio properties of G352.7–0.1), those authors estimated a value of 40 TeV for E_{max} .

An analysis of a pointed X-ray observation of G352.7–0.1 with the *XMM-Newton* Observatory (Turner et al. 2001) is presented by Giacani et al. (2009). The pn-CCD camera (Strüder et al. 2001) and the Multi-Object Spectrometer cameras (Turner et al. 2001) (hereafter referred to as the PN, MOS1 and MOS2 respectively for the remainder of this paper) aboard *XMM-Newton* comprise the European Photon Imaging Camera (EPIC). Based on the superior resolution attained by the PN, MOS1 and MOS2 in imaging G352.7–0.1, Giacani et al. (2009) disagreed with Kinugasa et al. (1998) (who had concluded that the X-ray morphology of G352.7–0.1 was shell-like, similar to its radio morphology) and instead classified the X-ray morphology as center-filled, therefore moti-

vating a classification of G352.7–0.1 as an MM-SNR. Giacani et al. (2009) conducted a spectral analysis of extracted PN, MOS1 and MOS2 spectra for the entire angular extent of G352.7–0.1: the extracted spectra were fit with an NEI model (the same model implemented by Kinugasa et al. (1998)) and the parameters of the fit to the spectra were broadly similar to those reported by Kinugasa et al. (1998). Specifically, Giacani et al. (2009) reported fit values of $kT \sim 1.9 \pm 0.2$ keV, $\tau = 4.5 \pm 0.5 \times 10^{10} \text{ cm}^{-3} \text{ s}$ and abundances for silicon and sulfur of 2.4 ± 0.2 and 3.8 ± 0.3 relative to solar, respectively. Giacani et al. (2009) also reported an overabundance of argon (4.7 ± 1.2 relative to solar) in the X-ray emitting plasma associated with G352.7–0.1, the first report of an overabundance of argon in the X-ray emitting plasma associated with this SNR. Giacani et al. (2009) also commented on the presence of an Fe K emission line at 6.46 ± 0.03 keV in the extracted spectra. Based on the fit values of these parameters and assuming a distance to this SNR of 7.5 kpc, Giacani et al. (2009) estimated the electron density of the plasma to be $n_e = 0.3 \text{ cm}^{-3}$, the age of the SNR to be $t \sim 4700$ yr, an X-ray emitting mass of $10 M_\odot$ and an explosion energy of 10^{50} ergs. Lastly, Giacani et al. (2009) found no X-ray counterparts to the radio sources WBH2005 352.775–0.153 and WBH2005 352.772–0.149.

In the present paper we present an imaging and spectroscopic analysis of the properties of G352.7–0.1 based on pointed X-ray observations made by *XMM-Newton* and the *Chandra* X-ray Observatory: the present work contains (to the best of our knowledge) the first analysis of the dataset from the *Chandra* observation of this SNR. The *XMM-Newton* and *Chandra* observations of G352.7–0.1, as well as the accompanying data reduction, are presented and described in Sections 2.1 and 2.2, respectively. In Sections 3.1 and 3.2 we present spatial and spectral analysis of the *XMM-Newton* and *Chandra* datasets, respectively. We discuss properties of this SNR in Section 4, where we compare our results with previously-published analysis of the SNR (in Section 4.1). We also calculate and discuss physical properties of G352.7–0.1 – including electron density, pressure and X-ray-emitting mass – in Section 4.2. In Section 4.3 we investigate whether the X-ray-emitting plasma associated with G352.7–0.1 is overionized

(as seen in the cases of other Galactic MMSNRs). A search for a neutron star associated with this SNR through an analysis of the spectral properties of hard unresolved X-ray sources seen in projection toward the interior of the SNR is described in Section 4.4. In Section 4.5 we present the discovery of infrared emission from G352.7–0.1 as observed by the *Spitzer Space Telescope* and in Section 4.6 we discuss this SNR within the context of other MMSNRs that feature ejecta-dominated X-ray-emitting plasmas. Finally, our conclusions are presented in Section 5.

2. Observations and Data Reduction

2.1. *XMM-Newton* Observations and Data Reduction

G352.7–0.1 was the subject of a pointed *XMM-Newton* observation made on 2002 October 3 with all three EPIC cameras: the Sequence Number of the observation was 0150220101 (PI: J. Hughes). The fields of view of the MOS1, MOS2 and PN are all approximately 30 arcminutes: therefore the entire angular extent of G352.7–0.1 was easily sampled by a single pointed observation. The observation was conducted with all three cameras in MEDIUM filter mode: in addition, the PN camera was in Full Frame mode. The angular resolution of the MOS1, MOS2 and PN are all approximately 6 arcseconds at 1 keV: at the same energy, the effective collecting areas are 922 cm^2 for the two MOS cameras and 1227 cm^2 for the PN camera. These three cameras are each nominally sensitive to photons with energies between 0.2 and 12.0 keV.

Data for the observation of G352.7–0.1 was obtained from the on-line *XMM-Newton* data archive¹. To reduce the data, standard tools in the HEASoft software package² (Version 6.12) and the Science Analysis System (SAS – Gabriel et al. (2004)) software package³ (Version 12.0.0) were used. Specifically, the SAS tools `emchain` and `mos – filter` were used to process data from the observations made by the MOS1 and the MOS2 cameras and to identify good-time intervals within the observations. Likewise, the SAS tools `enchain` and `pn – filter` were used to process data from

¹See <http://xmm.esac.esa.int/xsa/>.

²See <http://heasarc.gsfc.nasa.gov/>.

³See <http://xmm.esa.int/sas/>.

the observation made by the PN camera and to identify good time intervals within the observation. After filtering, the effective exposure times for the MOS1, MOS2 and PN observations of G352.7–0.1 were 28639 s, 28650 s and 16468 s, respectively. We extracted MOS1, MOS2 and PN spectra for both the entire SNR as well as the bright eastern region of the SNR. To perform the spectral extraction for both the source and background regions, we used the SAS tool `evselect` and the extracted spectra were grouped to a minimum of 25 counts per channel. Subsequently, the SAS tool `backscale` was used to compute the proper value for the BACKSCAL keyword in the extracted spectra. Finally, the SAS tools `rmfgen` and `arfgen` were used to generate the response matrix files (RMFs) and the ancillary response files (ARFs), respectively, for the spectra required for spectral fitting. An analysis of the *XMM-Newton* extracted spectra is presented in Section 3.1. In Table 2 we present a summary of the *XMM-Newton* observation of G352.7–0.1.

2.2. *Chandra* Observations and Data Reduction

G352.7–0.1 was the subject of a pointed observation made with the *Chandra* X-ray Observatory (Weisskopf et al. 2002) on 2004 October 6. The corresponding ObsID of this observation is 4652 (PI: J. Hughes) and the observation was made in VERY FAINT timed mode with the Advanced CCD Imaging Spectrometer (ACIS) at a focal plane temperature of -118.54 C. The ACIS is comprised of the ACIS-S and ACIS-I arrays of chips: each chip is approximately $8.3' \times 8.3'$ (see Garmire et al. (2003) for more details about the properties of the ACIS chips). The entire angular extent of the X-ray emitting plasma associated with G352.7–0.1 fits within the field of view of one of the ACIS chips (specifically the ACIS-S3 chip). This particular chip (which is back-illuminated) is sensitive to photons with energies ranging from 0.3 to 10.0 keV and the FWHM angular resolution of this camera at 1 keV is $0.5''$. Finally, the effective collecting area of the ACIS-S3 chip for photons with energies of 1.0 keV is 525 cm^2 .

Data for the *Chandra* observation was obtained from the on-line *Chandra* data archive⁴: to re-

duce the data, standard tools in the *Chandra* Interactive Analysis of Observations (CIAO⁵) software package Version 4.4 (CALDB Version 4.4.7) was used to reduce and analyze the data. The CIAO tool `chandra_repro` was run to reprocess the dataset and to perform all of the recommended data processing steps: these steps included the application of the latest temperature-dependent charge transfer inefficiency correction, the latest time-dependent gain-adjustment and the latest gain map. The tool also flags bad pixels (creating a new bad pixel file) and applies additional filters based on grades and proper status columns. Running this tool creates a new EVT2 file which we further filtered to exclude time periods of significant background flare activity. This particular filtering was accomplished using the CIAO tool `chips`⁶: after all of the filtering was applied, the effective exposure time of the processed EVT2 file was 44583 seconds. In Table 3 we present a summary of the *Chandra* observation of G352.7–0.1.

To perform a spectral analysis of the X-ray emitting plasma associated with G352.7–0.1, the tool `specextract` was used to generate spectral files – source spectra, background spectra, ARFs and RMFs – of both the entire SNR as well as several regions within the SNR. The extracted spectra were grouped to a minimum of 15 counts per channel. An analysis of all of the *Chandra*-extracted spectra is presented in Section 3.2. To reduce the effect of point source contamination of the extracted spectra, the CIAO tool `wavdetect` – a wavelet-based source algorithm (Freeman et al. 2002) – was used to identify unresolved sources detected by the *Chandra* observation and exclude them while analyzing the diffuse emission (as described below).

3. Analysis and Results

3.1. *XMM-Newton* Observations of G352.7–0.1: Imaging and Spectroscopy

In Figure 1 we present an *XMM-Newton* MOS1 image of G352.7–0.1. The image depicts emission detected for the energy range of 0.5 to 10.0 keV. The emission has been smoothed with a Gaussian

⁵See Fruscione et al. (2006) and <http://cxc.harvard.edu/ciao/>.

⁶See <http://cxc.harvard.edu/chips/index.html>.

⁴See <http://cda.harvard.edu/chaser/>.

with a radius of 10 arcseconds. Radio emission as detected by the Very Large Array (VLA) at a frequency of 1.4 GHz (Dubner et al. 1993; Giacani et al. 2009) is depicted with overlaying contours (this radio map was provided courtesy of Gloria Dubner and was published in Dubner et al. (1993)). The combined position of the background double radio sources WBH 2005 352.775–0.153 and WBH 2005 352.772–0.149 (as seen toward the eastern boundary of the main radio shell) is indicated in the figure. No significant X-ray emission is detected from these background radio sources (in agreement with the results of Giacani et al. 2009). In addition, no significant X-ray emission is detected from the radio lobe of the SNR seen toward the southwest. As noted by Giacani et al. (2009), the X-ray emission from G352.7–0.1 is seen inside the main radio shell, thus motivating its classification as a MM-SNR. The X-ray emitting plasma appears to be broadly uniform in brightness with the exception of a bright region seen toward the eastern edge.

MOS1, MOS2 and PN spectra were extracted from both the entire angular extent of the plasma as well as for the bright eastern region. The extraction region for the whole SNR was circular and approximately $2.4'$ in radius while the extraction region for the bright eastern region of the SNR was elliptical with semi-major and semi-minor axes of $1.3'$ and $0.6'$, respectively. The background spectrum was extracted from an annular region concentric with the extraction region for the whole SNR. This annular region had an inner radius corresponding to the radius of the source region for the whole SNR and an outer radius of $3.3'$. The locations of all of these spectral extraction regions are depicted in Figure 1. The three spectra for the whole SNR were fitted simultaneously using the thermal model VNEI: this model is a non-equilibrium collisional plasma model which assumes a constant temperature, a single ionization parameter and variable elemental abundances (Hamilton et al. 1983; Liedahl et al. 1995; Borkowski et al. 2001). The version of the VNEI model used in this paper (Version 1.1) implements updated calculations of ionization fractions using dielectronic recombination rates as provided by Mazzotta et al. (1998). The choice of the VNEI model (instead of the NEI model with elemental abundances frozen to solar values) is motivated by the prominent lines of silicon and

sulfur seen in the spectra (as shown in Figure 2 as well as previous X-ray spectral analysis conducted of this SNR by Kinugasa et al. (1998) and Giacani et al. (2009)). The VNEI model was multiplied by the PHABS model to account for photoelectric absorption along the line of sight to G352.7–0.1.

We obtain statistically-acceptable fits (with χ^2_ν values of ~ 1.2 or less) to the extracted MOS1+MOS2+PN spectra for both the whole SNR as well as the bright eastern region. In Table 4 we present a summary of the fit parameters for the fits to both regions: we note that the parameters of our fit for the spectra of the whole SNR are broadly similar to those presented by Giacani et al. (2009). Regarding the possible presence of spatial variations in the spectral properties, we find little difference between the derived fit parameters for the whole SNR compared to the bright eastern region. Therefore, this region appears to be simply a bright region of the thermal X-ray-emitting plasma instead of a pulsar wind nebula of a neutron star associated with G352.7–0.1 as one could assume based on the images. The lack of obvious spatial variations in the spectral properties of the plasma is also consistent with the results of Giacani et al. (2009), who searched and failed to detect any such variations. In Figure 2 we present the extracted MOS1+MOS2+PN spectra for the whole SNR (using the extraction regions for the source spectrum and the background spectrum as shown in Figure 1). In Figure 3 we present confidence contour plots for the fit with the PHABS×VNEI fit to the spectra of the whole SNR.

3.2. *Chandra* Observations of G352.7–0.1: Imaging and Spectroscopy

The superior angular resolution of the *Chandra* ACIS-S compared to the *XMM-Newton* MOS1, MOS2 and PN instruments allows us to perform a more detailed spatially-resolved X-ray spectroscopic study of G352.7–0.1. Our *Chandra* image of this SNR is presented in Figure 4 and in Figure 5 we follow the example of Giacani et al. (2009) and present images made of G352.7–0.1 at three different energy cuts – namely 1.7–2.0 keV, 2.3–2.6 keV and 3.1–3.3 keV – that correspond to known emission lines of silicon, sulfur and argon, respectively. We first extracted a spectrum for the entire SNR: we then divided the angular ex-

tent of the SNR into six different regions and extracted spectra from each region. Based on their apparent locations within the angular extent of G352.7–0.1, we denoted these smaller regions as “bottom,” “right,” “middle,” “left,” “top” and the “crescent” region (this latter region corresponds to emission seen in the space between the two radio loops seen to cleave at the western portion of the SNR). We note that the “left” region contains most of the “eastern region” considered previously in our *XMM-Newton* spectral analysis. A background spectrum was obtained using an elliptical region located north of the angular extent of G352.7–0.1 but still on the ACIS-S3 chip. The locations of the regions of spectral extraction are all shown in Figure 6. All of the spectra were extracted using the CIAO tool `specextract`: this tool generates all required spectral files, including the source spectra, background spectra and weighted ARFs and RMFs. When source and background spectral files were extracted, care was taken to exclude counts from the locations of unresolved sources (primarily background galaxies) found within the extraction regions. This was accomplished by running the CIAO source detection tool `wavdetect`. The locations of the sources detected by `wavdetect` were noted and counts from these locations were excluded when spectra were extracted. We will return to the point sources detected by `wavdetect` in Section 4.4 when we discuss the search for an X-ray-emitting neutron star associated with this SNR.

The spectra of all of the regions were fit with the same VNEI model (combined with a PHABS model for the photoelectric absorption) employed to fit the extracted *XMM-Newton* spectra as described in the previous section. Again, the abundances of silicon and sulfur in the VNEI model were thawed while the abundances of the other elements were left frozen to solar values. In Tables 5, 6 and 7 we summarize the results of our fits to all of the extracted *Chandra* spectra. In contrast to our results for the *XMM-Newton* spectra, a single VNEI component with enhanced silicon and sulfur abundances *cannot* adequately fit all of the extracted *Chandra* spectra: unsatisfactory fits (with values for χ^2_ν of more than 1.2) were obtained for the spectra of two of the smaller regions (namely the “top” and “left” regions) as well as the spectrum for the whole SNR. A single VNEI compo-

nent with the enhanced silicon and sulfur abundances is sufficient to fit the spectra of the “bottom,” “right,” “middle” and “crescent” regions. Inspection of the values for the parameters of the fits reveals a significant variation in spectral properties across the whole angular extent of the SNR. For example, we note that the fitted temperatures range from $kT \sim 0.8$ keV for the “bottom” region to $kT \sim 2.1$ keV for the “crescent” region. We also note that the fitted abundances of silicon and sulfur show a range of values as well: in every region we considered the abundances for these two elements are super-solar. In contrast to the work of Giacani et al. (2009), we find no evidence for an overabundance of argon in the spectra of any of the regions that we considered: when we allowed the abundance of argon to vary, there were no improvements in any of the values of χ^2_ν for any of the fits to any of the regions. We speculate that the *Chandra* observation of this SNR (unlike the *XMM-Newton* observation) did not detect enough photons with energies corresponding to the argon line feature to investigate the putative overabundance of this element in detail.

To obtain statistically acceptable fits to the spectra of the “left” region, the “top” region and the whole SNR, we added additional components to the spectral fits. We first added a single power law component but we failed to obtain statistically acceptable fits (with $\chi^2_\nu \leq 1.3$) to the spectra of the “left” region, the “top” region nor the whole SNR. We then added an NEI component to our PHABS×VNEI model: we left the abundance of this NEI component frozen to unity. As an alternative, we also tried fitting the spectrum with a PHABS×(VNEI+VNEI) model. In this case, we thawed the abundance of silicon in one VNEI component and thawed the abundance of sulfur in the other VNEI component (the abundances of all other elements were left frozen at values of unity). In both cases, with the addition of a second thermal component, we were able to obtain statistically acceptable fits to the spectra of the two individual regions as well as the SNR as a whole. In Tables 6 and 7 we present the results of these fits to the extracted spectra for these regions. In Figure 7 we present the *Chandra* spectrum of the diffuse emission of G352.7–0.1 as fit by the PHABS×(VNEI+NEI) model. We believe that the presence of this second component has

only manifested itself through the *Chandra* observation of G352.7–0.1 (but not the *XMM-Newton* observation of the SNR) due to the significantly lower background inherent in observations made with the ACIS.

4. Discussion

4.1. Physical Interpretation

We comment on the physical plausibility of these two models for interpreting the spectra of these regions. Regarding the fits obtained with the PHABS×(VNEI+VNEI) models, we note that in each case the sulfur-rich thermal component is implied to be close to thermal equilibrium while the silicon-rich thermal component is not. We are not aware of a physical mechanism where two different X-ray-emitting plasmas which are enriched in different elemental abundances featuring different ionization timescales co-existing with each other. We therefore regard this model as not physically plausible. In contrast, the PHABS×(VNEI+NEI) may be readily explained by a plausible model where the VNEI model fits emission from stellar ejecta while the NEI model fits emission from swept-up material. Certainly, the large normalization of this latter component implies that the amount of swept-up material associated with this SNR is enormous. We note that a large swept-up mass may be expected for MMSNRs like G352.7–0.1 which preferentially appear to be located near molecular clouds and appear to be interacting with these clouds as well. We quantify this amount of mass when we discuss the physical properties of G352.7–0.1 in the next section.

4.2. Physical Properties of G352.7–0.1

We now discuss the physical properties of G352.7–0.1 as implied by the parameters derived in fits to the extracted *Chandra* spectrum for the whole SNR. In our analysis we will follow the approaches applied by Pannuti et al. (2010) and Pannuti et al. (2014) to other X-ray-detected Galactic MMSNRs (namely HB 21 (G89.0+4.7), CTB 1 (G116.9+0.2), Kes 17 (G304.6+0.1), G311.5–0.3, G346.6–0.2 and CTB 37A (G348.5+0.1)). We first note that the normalizations \mathcal{N} of the thermal models are defined by the relation

$$\mathcal{N} = \frac{10^{-14}}{4\pi d^2} \int n_e n_p dV \quad (1)$$

where d is the distance to G352.7–0.1 (assumed to be 7.5 kpc), n_e and n_p are the electron and proton number densities (respectively) and V is the volume of the SNR. We will assume that $n_e = 1.2 n_p$ and that the filling factor of the X-ray-emitting gas is unity (based on the uniform morphology of the diffuse emission). From this relation we can calculate the values for n_e and – by extension – n_p as well as the X-ray emitting mass M of the diffuse emission. Another important physical parameter to consider is the corresponding pressure P of the SNR. If we define the total number density of particles n_{total} to be the sum of the number densities of electrons, protons and helium nuclei (that is, $n_{total} = n_e + n_p + n_{He}$), we can make the approximation $n_{total} \approx 2 n_e$ for a plasma with cosmic abundances. Therefore, we may express P as

$$P/k = 2n_e T \text{ K cm}^{-3}, \quad (2)$$

where k is Boltzmann’s constant and T is the temperature of the SNR expressed in Kelvin. Finally, we estimate the age t of G352.7–0.1 using the same relation employed by Giacani et al. (2009) (see Section 1), that is,

$$t \sim \tau/n_e. \quad (3)$$

where τ is the ionization timescale of the X-ray-emitting plasma (see Borkowski et al. (2001)).

We first calculate values for n_e for both the ejecta-dominated component and the ISM-dominated component using the normalizations obtained when using the PHABS×(VNEI+NEI) model to fit the extracted *Chandra* spectrum of the whole SNR (see Table 6). If we approximate the volume of G352.7–0.1 to be a spheroid with radii of 2.4 arcmin × 2.1 arcmin × 2.3 arcmin (corresponding to radii of 5.2 pc × 4.6 pc × 5.0 pc at the assumed distance of 7.5 kpc to the SNR), the corresponding volume of the SNR is $\sim 1.1 \times 10^{58} \text{ cm}^3$. Using Equation 1, we calculate (for the ejecta-dominated component) an electron density $n_e = 0.33 \text{ cm}^{-3}$, a proton density $n_p = 0.28 \text{ cm}^{-3}$ and an X-ray emitting mass of $M_X = n_e \times n_p \times V = 2.6 M_\odot$. Applying the same equation to the ISM-dominated component, we calculate $n_e = 6.0$

cm^{-3} , $n_p = 4.9 \text{ cm}^{-3}$ and $M_X = 45 M_\odot$. While the calculated X-ray emitting mass for the ejecta-dominated component of the SNR is comparable to that seen for other Galactic SNRs, the X-ray emitting-mass for the ISM-dominated component of the SNR is remarkably large. For comparison purposes, Rho & Borkowski (2002) estimated that the swept-up X-ray-emitting mass associated with the MM SNR W28 was only $\sim 20\text{--}25 M_\odot$. From Equation 2, we calculate corresponding pressures of the ejecta-dominated component and the ISM-dominated components to be $2.5 \times 10^7 \text{ cm}^{-3} \text{ K}$ and $3.3 \times 10^7 \text{ cm}^{-3} \text{ K}$, respectively. These two values are nearly three orders of magnitude greater than the typical ISM pressure. We then use Equation 3 to estimate the age of the SNR to be $t \sim 1.7 \times 10^{10} \text{ cm}^{-3} \text{ s} / 0.33 \text{ cm}^{-3} \sim 1600$ years. Finally, we estimate the initial explosion energy E_{SN} of this supernova using the well-known Sedov equation (Sedov 1959)

$$E_{SN} = \frac{r^5 \rho}{t^2}. \quad (4)$$

Assuming an age $t=1600$ years, a radius $r=4.9$ pc and a mass density $\rho = n_p m_p$ (where $n_p = 4.6 \text{ cm}^{-3}$ and m_p is the mass of a proton), we calculated $E_{SN} = 2.54 \times 10^{51}$ ergs.

We now compare our computed physical parameters to those determined by Giacani et al. (2009). Our estimate of the electron number density n_e for the ejecta-dominated component is quite similar to the value derived for that parameter by those authors. Our estimate of the swept-up mass is higher than that calculated by Giacani et al. (2009) while our age estimate is less than half the age derived by those authors and is comparable to the age estimate given by Kinugasa et al. (1998). Our estimate of the initial explosion energy is also an order of magnitude greater than the estimates of the initial explosion energy provided by Giacani et al. (2009) and Kinugasa et al. (1998). We attribute differences in part to our use of two thermal components while fitting the extracted *Chandra* spectra while Giacani et al. (2009) only used a single component to fit the extracted *XMM-Newton* spectra.

4.3. Is the X-ray Emitting Plasma Associated With G352.7–0.1 Overionized?

We now investigate whether the X-ray-emitting plasma associated with G352.7–0.1 is overionized.

Here, overionization means that atomic species are observed to be in a higher ionization state than expected based on the observed electron temperature of the X-ray-emitting plasma. Several Galactic MMSNRs are known to feature overionized X-ray-emitting plasmas: examples of such MMSNRs include IC 443 (Yamaguchi et al. 2009), W49B (Ozawa et al. 2009), G346.6–0.2 (Yamauchi et al. 2012) and G359.0–0.1 (Ohnishi et al. 2011). Reviews of the phenomenon of overionized X-ray-emitting plasmas associated with SNRs is provided by Miceli et al. (2011) and Vink (2012).

To investigate whether or not the X-ray-emitting plasma associated with G352.7–0.1 is indeed over ionized, we follow the analysis presented by Yamauchi et al. (2012). Using the SPEX software package (Kaastra et al. 1996), those authors fitted the *Suzaku* XIS spectra of the SNR G346.6–0.2 using the *neij* model. According to this model (see Yamauchi et al. (2012)), an X-ray emitting plasma may be described such that the initial ion temperature kT_Z and the original electron temperature kT_{e1} were the same (that is, $kT_Z = kT_{e1}$) and the plasma itself was in collisional ionization equilibrium. Over time, the electron temperature drops to kT_{e2} due to rapid electron cooling. Such a model can reflect accurately a rapid electron cooling as predicted in models of SNR evolution.

We used the SPEX (Version 2.03.03) tool *trafo* (Version 1.02) to convert the extracted *Chandra* spectral files for the whole SNR into *.spo* files suitable for analysis by the software package. We attempted to fit with the *neij* model by adopting a value of 5 keV for the initial electron temperature kT_{e1} (similar to the procedure taken by Yamauchi et al. (2012)), freezing kT_{e1} to this value and thawing the abundances of silicon and sulfur while allowing the other fit parameters (N_H , normalization, kT_{e2} , kT_Z and τ) to vary. We were unable to generate a statistically-acceptable fit using the *neij* model that is superior (that is, with a lower value for χ^2_ν) than that obtained for the thermal models described above. We therefore conclude that the X-ray emitting plasma associated with G352.7–0.1 is not overionized.

4.4. Search for Unresolved X-ray Sources

We next conducted a search for a neutron star associated with G352.7–0.1, taking advantage of

the high angular resolution capabilities of *Chandra*. To the best of our knowledge, it is the first search for the neutron star in G352.7–0.1. As noted above, G352.7–0.1 is suspected to be interacting with molecular clouds based on the detection of maser emission: such a result suggests (but does not prove) that the stellar progenitor of G352.7–0.1 was formed near a molecular cloud and is massive. Another robust argument for a massive stellar progenitor associated with this SNR is the large calculated swept-up mass of $45 M_{\odot}$ coupled with the X-ray-emitting ejecta mass of $2.6 M_{\odot}$. Therefore, a search for the neutron star produced in the same supernova explosion that parented this SNR is warranted. There is also a possibility that the supernova explosion that produced G352.7–0.1 may also have fostered a black hole (see e.g., Kaplan et al. (2004, 2006) for the discussion of the non-detections of compact objects in several other SNRs).

To conduct our search, we used the CIAO tool `dmcopy` to create an event list and a “hard” image for the energy range from 2.0 to 10.0 keV. We then ran the CIAO tool `wavdetect` – a wavelet-based unresolved source detection tool (Freeman et al. 2002) – with its default parameters on this image to find unresolved sources seen within the apparent angular extent of G352.7–0.1. In Figure 8 we present our hard image of G352.7–0.1 with the locations of the unresolved sources detected by `wavdetect` indicated. Six unresolved sources were detected by this tool at a minimum of a $S/N \gtrsim 4$ level and properties of these sources are listed in Table 8. For the two brightest detected sources, we performed spectral fitting in XSPEC using an absorbed power law model with N_H fixed at $2.6 \times 10^{22} \text{ cm}^{-2}$ (the average Galactic value in this direction for $d \sim 7.5$ kpc). Due to the small number of counts we did not bin the data and used C-statistics while performing the fits. Sources 1 and 2 both show extremely hard (albeit uncertain) spectra with $\Gamma = -0.4 \pm 0.3$ and $\Gamma = -0.5 \pm 0.4$, respectively. If N_H is allowed to be free, its value increases by a factor of two compared to the frozen value (for both sources) and the photon indices become $\Gamma \sim 0.3$ and $\Gamma \sim 0.1$, respectively. These parameters are, however, poorly constrained due to the small total number of counts detected from each source, especially at energies below 2 keV. Since it is unlikely for the Galactic N_H to be

even larger⁷, the spectra of these sources must also be intrinsically hard. Such hard spectra are unusual for young isolated neutron stars or pulsars, while the large X-ray to near-infrared (K-band) flux ratio ($\gtrsim 30$ in K-band) implies that both sources are likely to be either heavily obscured (that is, the soft component is completely absorbed) magnetic cataclysmic variables (CVs) in the hard state, obscured remote high mass X-ray binaries (HMXBs) in the low-hard state or AGNs. The rest of the sources in Table 8 have even fewer counts which precludes any spectral analysis in the X-ray. Sources 5 and 6 have counterparts detected in the near-infrared (by 2MASS) and/or infrared (by the *Spitzer* GLIMPSE survey), therefore neither of them can be an isolated pulsar or neutron star related to G352.7–0.1. Finally, very little information is available about sources 3 and 4. The lack of near-infrared and infrared counterparts for these sources coupled with their hard band X-ray luminosities ($\simeq 10^{32} \text{ erg s}^{-1}$ at $d = 7.5$ kpc) are in principle consistent with those of isolated pulsars at this distance. Indeed, as shown in the top panel in Figure 3 from Kargaltsev et al. (2013), the scatter in the X-ray efficiencies ($\eta_X = L_X / \dot{E}$) of young (characteristic ages $t \lesssim 10$ kyr; spin-down energy-loss rates $\dot{E} \gtrsim 10^{37} \text{ erg s}^{-1}$) pulsars is nearly 5 orders of magnitude. Therefore, $L_X \simeq 10^{32} \text{ erg s}^{-1}$ can be accommodated by assuming low efficiency $\eta_X \lesssim 10^{-4}$ (although the number of known pulsars exhibiting such low efficiencies is fairly small). Alternatively, Sources 3 and 4 may be remote faint AGNs whose soft X-ray and optical and near-infrared emission is severely attenuated by the large absorbing column along this line of sight.

We also comment on the possibility that a compact central object (CCO) could be associated with G352.7–0.1. CCOs are a type of isolated NSs which are found in the centers of their host SNRs. They exhibit purely thermal emission (with surface temperatures of $kT \sim 0.2\text{--}0.4$ keV) and feature luminosities of $L_X \times 10^{33} \text{ erg s}^{-1}$ over the 0.5 to 8 keV energy range (de Luca 2008). Therefore, Source 3 could be an absorbed CCO associated with G352.7–0.1. Alternatively, if G352.7–0.1 is further away than the assumed 7.5 kpc, the CCO

⁷The average Galactic HI column density in this direction is $(1.4\text{--}1.6) \times 10^{22} \text{ cm}^{-2}$ – see Dickey & Lockman (1990).

(if it exists) may not be detectable in the existing *XMM-Newton* and *Chandra* datasets.

Since none of these six sources appears to be a particularly promising candidate for a compact object associated with G352.7–0.1, there remains an open question about the presence of a compact object leftover from the SN explosion (assuming it was indeed a core-collapse supernova and not a Type Ia supernova). The remaining option would be an isolated black hole which can be difficult to detect because of the very low accretion rate (assuming Bondi-Hoyle accretion) inside the rarefied hot gas filling the interior of the SNR (Beskin & Karpov 2005).

We also note that none of the sources detected by *wavdetect* at a signal-to-noise ratio of four or greater are physically coincident with the radio sources WBH2005 352.775-0.153 and WBH2005 352.772-0.149 seen toward the eastern rim of the SNR and speculated to be associated with a distant AGN (see Section 1). We therefore place an upper limit of $\sim 10^{-16}$ ergs cm $^{-2}$ s $^{-1}$ on the absorbed X-ray fluxes from these two radio sources.

4.5. Infrared Emission from G352.7–0.1

We have searched for an infrared counterpart to G352.7–0.1 by examining archival observations of the field that includes this SNR. We find a counterpart from data collected at a wavelength of 24 μ m made with the Multiband Imaging Photometer (MIPS – Rieke et al. (2004)) aboard the *Spitzer Space Telescope* (Werner et al. 2004) as part of the MIPS GAL survey that sampled the inner Galactic plane at the wavelengths of 24 μ m and 70 μ m (Carey et al. 2009). In Figure 5, we present three images of G352.7–0.1 at different wavelengths – namely a broadband (0.5 – 8.0 keV) X-ray image made with *Chandra*, an infrared 24 μ m image made with MIPS aboard *Spitzer* and a radio continuum 6cm map made with the VLA. As we previously mentioned, one can clearly see the contrasting center-filled X-ray morphology and shell-like radio morphology that categorize G352.7–0.1 as an MMSNR. Also note in these images the strong correlation between the regions of infrared emission and regions of radio emission. At both wavelengths, a nearly complete inner ring of emission is seen along with an outer incomplete ring of emission seen toward the southeast. A study of fourteen Galactic SNRs de-

tected by MIPS was presented by Andersen et al. (2011). Those authors found evidence for interactions between these SNRs and adjacent molecular clouds based on the detection of [O I] emission ionic lines and emission from molecular lines. We suspect that the observed flux as detected by MIPS from G352.7–0.1 probably has a very similar origin. We also note that – like all of the sources considered in the survey conducted by Andersen et al. (2011) – G352.7–0.1 is an MMSNR. We therefore argue that the detection of infrared emission from this SNR helps strengthen the link between MMSNRs and SNRs interacting with adjacent molecular clouds. In a recent work (Panuti et al. 2014), we found additional evidence for this link in a study of the X-ray properties of four Galactic MMSNRs that were detected by *Spitzer* at shorter infrared wavelengths (such as 4.5 μ m) with the Infrared Array Camera (IRAC – Fazio et al. (2004)) in the survey conducted by Reach et al. (2006).

4.6. G352.7–0.1: An Ejecta-Dominated Mixed-Morphology SNR

In Table 9 we provide a list of known Galactic MMSNRs which are known to feature ejecta-dominated X-ray emission. By “ejecta-dominated,” we mean that the measured abundances of certain elements (metals) are elevated relative to solar abundances. Examples of such elements are silicon and sulfur, which are seen to be elevated in the X-ray-emitting plasmas of MMSNRs: in Table 9 we list examples of sources of this type. As shown in this paper and in previous analyses conducted by Kinugasa et al. (1998) and Giacani et al. (2009), G352.7–0.1 (similar to HB 21 and G359.1–0.1) features silicon and sulfur abundances that exceed solar.

The origin of ejecta-dominated emission from MMSNRs remains elusive. Estimates of the ages of MMSNRs often hover near $\sim 10^4$ years. For such ages, the X-ray-emitting plasma associated with an SNR is expected to be dominated by the swept-up ISM rather than ejecta with elemental abundances comparable to solar. Ejecta-dominated MMSNRs appear to represent a new evolutionary scenario through which sources of this type are formed. As summarized by Vink (2012), a high metal content in the X-ray emitting plasma may help explain the observed emission characteristics

of MMSNRs for two reasons. Firstly, metal-rich plasmas produce more X-ray emission than plasmas which are not metal-enhanced: this leads to a contrast between the X-ray emitting metal-rich interior and the metal-poor swept-up exterior of the SNR. Secondly, the uniform temperatures in the interiors of MM SNRs can be explained using thermal conduction models (Cox et al. 1999): this explanation is challenged by magnetic fields limiting thermal conduction along magnetic field lines, but if the interiors of MM SNRs are dominated by ejecta, then the stellar magnetic field may be reduced due to the expansion and is thus significantly weakened (to values as low as 10^{-14} G – see Vink (2012)). At such a low value conduction across field lines becomes as efficient as conduction along field lines: thus thermal conduction becomes efficient in these conditions but only to the boundaries between the ejecta-dominated matter and swept-up matter. At these boundaries, Rayleigh-Taylor instabilities may contain magnetic fields with elevated strengths, thus hampering efficient thermal conduction.

Of the SNRs listed in Table 9, the only two which may possibly host neutron stars are CTB 1 (Pannuti et al. 2010) and IC 443. However, in the case of IC 443, the observed neutron star is unlikely to be associated with the SNR because it is observed to move in the wrong direction (that is, toward the center of the SNR). Therefore, it may be that MMSNRs are such that after the explosion, their progenitors do not leave a neutron star: either a black hole is produced or nothing is left. If the ejecta mass is large, then it is likely that the progenitor star was a massive star and a black hole was left behind. Such progenitors may explain the elevated abundances in MMSNRs and the fact that they are close to molecular clouds (where massive stars are formed more easily).

We have searched for other characteristics that the SNRs listed in Table 9 may have in common. For example, we considered whether the radio morphologies of these SNRs are all similar, such as bilateral (also known as “barrel-shaped” – see Kesteven & Caswell (1987)): examples of well-known barrel-shaped Galactic SNRs include G296.5+10.0 (Storey et al. 1992) and G320.4–1.2 (Dubner et al. 2002). In fact, in a seminal study of Galactic SNRs presented by Kesteven & Caswell (1987) that classified these sources based on their

radio morphologies did indeed identify one of the SNRs in Table 9 – namely CTB 1 – as a “well-developed” barrel: other SNRs like W44, HB21, HB3, IC 443, and Kes 27 were described as “difficult to classify” by those authors. More recently, Keohane et al. (2007) argued that the SNR W49B should be classified as a barrel-shaped SNR (it had been classified as a “possible barrel” by Kesteven & Caswell (1987)). More detailed radio observations and analysis need to be conducted of these SNRs (and the sample of known ejecta-dominated mixed-morphology SNRs must be increased) to determine if barrel-shape morphology is consistently seen amongst these sources.

5. Conclusions

The conclusions of this paper may be summarized as follows:

- 1) Complementary *XMM-Newton* and *Chandra* observations of the Galactic SNR G352.7–0.1 confirm a center-filled thermal morphology with a contrasting shell-like radio morphology. These observations motivate a classification of this source as a MMSNR.
- 2) Analysis of extracted *XMM-Newton* spectra for the whole SNR and for the bright eastern region can be fit satisfactorily with a single thermal component that describes an X-ray-emitting plasma that is not in collisional ionization equilibrium with enhanced abundances of silicon and sulfur. This result is consistent with previous analysis of extracted *ASCA* and *XMM-Newton* spectra of this SNR. In contrast, analysis (presented here for the first time) of extracted *Chandra* spectra of the whole SNR as well as separate regions of the SNR cannot all be fit satisfactorily with a single thermal component. In the cases of the “left” and “top” regions as well as the whole SNR, statistically-acceptable fits are obtained when either a second thermal component with solar abundances is added or when two thermal components with different temperatures (one with enhanced silicon abundance and the other with enhanced sulfur abundance). We argue that the former scenario is more physically plausible.
- 3) We have calculated physical parameters (computed based on our derived fit parameters) for G352.7–0.1, include n_e , n_p , P , M and t . Most notably, our computed masses of the X-ray-emitting

masses of the ejecta-dominated component and the ISM-dominated component are $2.6 M_{\odot}$ and $45 M_{\odot}$, respectively. This is a remarkably high swept-up mass for a Galactic SNR and may indicate a unique evolutionary scenario (involving a massive progenitor star interacting with a dense molecular cloud environment) for this SNR.

4) We have conducted a spectral analysis of the extracted *Chandra* spectrum of the whole SNR to determine if the X-ray emitting plasma associated with this SNR is over-ionized. We cannot obtain a satisfactory fit to the extracted spectrum using the *nei* model with parameters that might indicate over-ionization: we therefore conclude that the X-ray emitting plasma associated with G352.7–0.1 is not over-ionized.

5) We have searched for a hard unresolved X-ray source that may be the neutron star associated with G352.7–0.1. We find six unresolved X-ray sources seen in projection toward the interior of the SNR but none of these sources may be firmly classified as a neutron star physically associated with G352.7–0.1. We also find no X-ray counterparts to the background radio galaxy (with prominent radio lobes) seen in projection toward the eastern rim of the SNR.

6) We have presented for the first time the detection of infrared emission (namely emission detected at $24 \mu\text{m}$ by MIPS aboard *Spitzer*) from this SNR. The infrared morphology is shell-like and strongly resembles the radio morphology, including the complete inner radio shell and incomplete outer radio shell. Such emission has been detected previously from SNRs known to be interacting with adjacent molecular clouds: this detection helps confirm that G352.7–0.1 is indeed interacting with an adjacent molecular cloud.

7) We have compared G352.7–0.1 to other ejecta-dominated MMSNRs. The origin of ejecta-dominated emission from MMSNRs remains unknown and may indicate a new scenario for the evolution of this class of source.

We thank the referee for helpful comments and suggestions that have improved the quality of this manuscript. This research has been supported by a grant from the Kentucky Space Grant Consortium. O.K. acknowledges support from archival *Chandra*/NASA award AR3-14017X. T.G.P. thanks Jelle de Plaa for his assistance with

installing and using the SPEX software package: he also thanks Keith Arnaud for helpful assistance in the use of the XSPEC software package. T.G.P. also thanks David Alex May and Tiffany Murray for their assistance in reducing the *Chandra* data for G352.7–0.1. We also thank Gloria Dubner for kindly sharing her radio maps of G352.7–0.1 with us. This research has made use of NASA’s Astrophysics Data System and the NASA/IPAC Extragalactic Database (NED) which is operated by the Jet Propulsion Laboratory, California Institute of Technology, under contract with the National Aeronautics and Space Administration. This research has also made use of data obtained from the *Chandra Data Archive* and software provided by the *Chandra X-ray Center* (CXC) in the application packages *CIAO* and *ChIPS*. Finally, this work is based on observations obtained with *XMM-Newton*, an ESA science mission with instruments and contributions directly funded by ESA Member States and the USA (NASA).

REFERENCES

- Andersen, M., Rho, J., Reach, W. T., Hewitt, J. W. and Bernard, J. P. 2011, *ApJ*, 742, 7
- Beskin, G. M. & Karpov, S. V. 2005, *A&A*, 440, 223
- Borkowski, K. J., Lyerly, W. J. & Reynolds, S. P. 2001, *ApJ*, 548, 820
- Burke, B. E., Mountain, R. W., Daniels, P. J., Cooper, M. J. & Dolat, V. S. 1994, *IEEE Trans. Nuclear Science*, 41, 375
- Carey, S. J. et al. 2009, *PASP*, 121, 76
- Caswell, J. L., Haynes, R. F., Milne, D. K. & Wellington, K. J. 1983, *MNRAS*, 203, 595
- Chen Y., Seward, F. D., Sun, M. & Li, J. 2008, *ApJ*, 676, 1040
- Clark, D. H., Caswell, J. L. & Green, A. J. 1973, *Nature*, 246, 28
- Clark, D. H., Caswell, J. L. & Green, A. J. 1975, *AuJPA*, 37, 1
- Cox, D. P. et al. 1999, *ApJ*, 524, 179

- de Luca, A. 2008, 40 Years of Pulsars: Millisecond Pulsars, Magnetars and More, 2008, AIPC, 983, 311
- Dickey, J. M. & Lockman, F. J. 1990, ARA&A, 28, 215
- Dubner, G. M., Moffett, D. A., Goss, W. M. & Winkler, P.F. 1993, AJ, 105, 2251
- Dubner, D. M., Gaensler, B. M., Giacani, E.B., Goss, W. M. & Green, A. J. 2002, AJ, 123, 337
- Fazio, G. G. et al. 2004, ApJS, 154, 10
- Freeman, P. E., Kashyap, V., Rosner, R. & Lamb, D. Q. 2002, ApJS, 138, 185
- Fruscione, A. et al., 2006, Proc. SPIE, 6720
- Gabriel, C. et al. 2004, Astronomical Data Analysis Software and Systems (ADASS), XIII, 314, 759
- Garmire, G. P., Bautz, M. W., Ford, P. G., Nousek, J. A. & Ricker, G. R. Jr., 2003, Proc. SPIE, 4851, 28
- Giacani, E., Smith, M. J. S., Dubner, G., Loiseau, N., Castelletti, G. & Paron, S. 2009, A&A, 507, 841
- Green, A. J., Frail, D. A., Goss, W. M. & Otrupcek, R. 1997, AJ, 114, 2058
- Green, D. A., 2009a, 'A Catalogue of Galactic Supernova Remnants (2009 March version)', Astrophysics Group, Cavendish Laboratory, Cambridge, United Kingdom (available at "<http://www.mrao.cam.ac.uk/sureys/snrs/>").
- Green, D. A. 2009b, BASI, 37, 45
- Hamilton, A. J. S., Sarazin, C. L. & Chevalier, R. A. 1983, ApJS, 51, 115
- Jansen, F. et al. 2001, A&A, 365, L1
- Kaastra, J. S., Mewe, R. & Nieuwenhuijzen, H. 1996, UV and X-ray Spectroscopy of Astrophysical and Laboratory Plasmas, ed. K. Yamashita and T. Watanabe (Universal Academy Press, Tokyo), p. 411
- Kaplan, D. L., Frail, D. A., Gaensler, B. M., Gotthelf, E. V., Kulkarni, S. R., Slane, P. O. & Nechita, A. 2004, ApJS, 153, 269
- Kaplan, D. L., Gaensler, B. M., Kulkarni, S. R. & Slane, P. O. 2006, ApJS, 163, 344
- Kargaltsev, O., Pavlov, G. G. & Durant, M. 2013, ASPC, 466, 167
- Keohane, J. W., Reach, W. T., Rho, J. & Jarrett, T. H. 2007, ApJ, 654, 938
- Kesteven, M. J. & Caswell, J. L. 1987, A&A, 183, 118
- Kinugasa, K., Torii, K., Tsunemi, H., Yamauchi, S., Koyama, K. & Dotani, T. 1998, PASJ, 50, 249
- Koralesky, B., Frail, D. A., Goss, W. M., Claussen, M. J. & Green, A. J. 1998, AJ, 116, 1323
- Lazendic, J. S. & Slane, P. O., 2006, ApJ, 647, 350
- Liedahl, D. A., Osterheld, A. L. & Goldstein, W. H. 1995, ApJ, 438, L115
- Makishima, K., Tashiro, M., Ebisawa, K., Ezawa, H., Fukazawa, Y., Gunji, S., Hirayama, M., Ide-sawa, E. et al. 1996, PASJ, 48, 171
- Mazzotta, P., Mazzitelli, G., Colafrancesco, S. & Vittorio, N. 1998, A&AS, 133, 403
- Miceli, M. 2011, MmSAI, 82, 709
- Ohashi, T., Ebisawa, K., Fukazawa, Y., Hiyoshi, K., Horii, M., Ikebe, Y., Ikeda, H., Inoue, H. et al. 1996, PASJ, 48, 157
- Ohnishi, T., Koyama, K., Tsuru, T. G. et al. 2011, PASJ, 63, 257
- Ozawa, M., Koyama, K., Yamaguchi, H., Masai, K. & Tamagawa, T. 2009, ApJ, 706, L71
- Pannuti, T. G., Rho, J., Borkowski, K. J. & Cameron, P. B. 2010, AJ, 140, 1787
- Pannuti, T. G., Rho, J., Heinke, C. O. & Moffitt, W. P. 2013, AJ, in press (arXiv:1312.3929)
- Reach, W. T., Rho, J., Tappe, A., Pannuti, T. G., Brogan, C. L., Churchwell, E. B., Meade, M. R., Babler, B. et al. 2006, AJ, 131, 1479
- Rieke, G. H. et al. 2004, ApJS, 154, 25
- Reynolds, S. P. & Keohane, J. W. 1999, ApJ, 525, 368

- Rho, J. & Petre, R. 1998, *ApJ*, 503, L167
- Rho, J. & Borkowski, K. J. 2002, *ApJ*, 575, 201
- Sedov, L. I., *Similarity and Dimensional Methods in Mechanics*, New York: Academic Press, 1959.
- Serlemitsos, P. J., Jalota, L., Soong, Y., Kuneida, H., Tarawa, Y., Tsusaka, Y., Suzuki, H., Sakima, Y. et al. 1995, *PASJ*, 47, 105
- Shelton, R. L., Kuntz, K. D. & Petre, R. 2004, *ApJ*, 611, 906
- Storey, M. C., Staveley-Smith, L., Manchester, R. N. & Kesteven, M. J. *A&A*, 265, 752
- Strüder, L. et al. 2001, *A&A*, 365, L18
- Sugizaki, M., Mitsuda, K., Kaneda, H., Matsuzaki, K., Yamauchi, S. & Koyama, K. 2001, *ApJS*, 134, 77
- Tanaka, Y., Inoue, H. & Holt, S. S. 1994, *PASJ*, 46, L37
- Toledo-Roy, J. C., Velázquez, P. F., Esquivel, A. & Giacani, E. 2014, *MNRAS*, 437, 898
- Troja, E., Bocchino, F., Miceli, M. & Reale, F. 2008, *A&A*, 485, 777
- Turner, M. J. L. et al. 2001, *A&A*, 365, L27
- Vink, J. 2012, *A&ARv*, 20, 49
- Weisskopf, M. C., Brinkman, B., Canizares, C., Garmire, G., Murray, S. & van Speybroeck, L. P. 2001, 114, 1
- Werner, M. W. et al. 2004, *ApJS*, 154, 1
- White, R. L. & Long, K. S. 1991, *ApJ*, 373, 543
- White, R. L., Becker, R. H. & Helfand, D. J. 2005, *AJ*, 130, 586
- Whiteoak, J. B. Z. & Green, A. J. 1998, *A&AS*, 118, 329
- Yamaguchi, H., Ozawa, M., Koyama, K., et al. 2009, *ApJ*, 705, L6
- Yamaguchi, H., Tanaka, M., Maeda, K., Slane, P. O., Foster, A., Smith, R. K., Katsuda, S. & Yoshii, R. 2012, *ApJ*, 749, 137
- Yamauchi, S., Nobukawa, M., Koyama, K. and Yonemori, M. 2012, *PASJ*, 65, 6

TABLE 1
GENERAL PROPERTIES OF G352.7–0.1

Property	Value	References
R.A. (J2000.0)	17 27 40	(1)
Decl. (J2000.0)	−35 07	(1)
Angular Diameters (arcmin×arcmin)	8×6	(1)
Distance (kpc)	7.5±0.5	(2)
Physical Diameters (pc)	17×13	(3)
Flux Density at 5000 MHz (Jy)	2.3	(4)
Flux Density at 1465 MHz (Jy)	3.4±0.4	(5)
Flux Density at 1415 MHz (Jy)	4.7	(6)
Flux Density at 1400 MHz (Jy)	3.1±0.3	(7)
Flux Density at 843 MHz (Jy)	4.4	(8)
Flux Density at 408 MHz (Jy)	9.6	(4)
Spectral Index α ($S_\nu \propto \nu^\alpha$)	−0.6	(5)

NOTE.—References: (1) – Green (2009a), (2) – Giacani et al. (2009), (3) – This paper, (4) – Clark et al. (1975), (5) – Dubner et al. (1993), (6) – Caswell et al. (1983), (7) – Giacani et al. (2009), (8) – Whiteoak & Green (1996).

TABLE 2
SUMMARY OF *XMM-Newton* MOS1, MOS2 AND PN OBSERVATIONS OF G352.7-0.1

Sequence Number	Observation Date	R.A. (J2000.0)	Decl. (J2000.0)	MOS1 Effective Exposure Time (s)	MOS1 Count Rate (counts s ⁻¹)	MOS2 Effective Exposure Time (s)	MOS2 Count Rate (counts s ⁻¹)	PN Exposure Time (s)	PN Effective Count Rate (counts s ⁻¹)
0150220101	2002 October 3	17 27 35.0	-35 07 23	28639	9.2×10^{-2}	28650	9.3×10^{-2}	16468	2.3×10^{-1}

NOTE.—The units of Right Ascension are hours, minutes and seconds while the units of Declination are degrees, arcminutes and arcseconds. Count rates are for the entire angular extent of the diffuse emission and correspond to the energy range from 1.0 keV to 5.0 keV.

TABLE 3
SUMMARY OF *Chandra* ACIS-S OBSERVATION OF G352.7–0.1

Sequence Number	ObsID	Observation Date	R.A. (J2000.0)	Decl. (J2000.0)	Roll (deg)	ACIS-S Effective Exposure Time (s)	ACIS-S Count Rate (s)
500471	4652	2004 October 6	17 27 41.0	–35 06 45	263	44583	1.4×10^{-1}

NOTE.—The units of Right Ascension are hours, minutes and seconds while the units of Declination are degrees, arcminutes and arcseconds. Count rates are for the entire angular extent of the diffuse emission and correspond to the energy range from 1.0 keV to 5.0 keV.

TABLE 4
SUMMARY OF *XMM-Newton* MOS1+MOS2+PN SPECTRAL ANALYSIS OF G352.7–0.1
(PHABS×VNEI MODEL)

Parameter	Eastern Region	Whole SNR
N_H (10^{22} cm $^{-2}$)	$2.46^{+0.56}_{-0.46}$	$2.78^{+0.24}_{-0.28}$
kT (keV)	$1.90^{+1.60}_{-0.70}$	$1.20^{+0.34}_{-0.24}$
τ (10^{10} cm $^{-3}$ s)	$3.57^{+3.43}_{-1.57}$	$4.07^{+2.53}_{-1.17}$
Si	$2.6^{+1.5}_{-0.9}$	$2.3^{+0.6}_{-0.4}$
S	$4.5^{+3.5}_{-1.7}$	$3.5^{+1.4}_{-0.8}$
Normalization (cm $^{-5}$)	4.9×10^{-4}	3.5×10^{-3}
χ^2_ν (χ^2/DOF)	1.19 (84.58/71)	1.15 (444.17/387)
Absorbed Flux (ergs cm $^{-2}$ s $^{-1}$)	2.4×10^{-13}	8.4×10^{-13}
Unabsorbed Flux (ergs cm $^{-2}$ s $^{-1}$)	1.3×10^{-12}	6.4×10^{-12}
Unabsorbed Luminosity (ergs s $^{-1}$)	8.8×10^{33}	4.3×10^{34}

NOTE.—All stated error bounds correspond to 90% confidence intervals. Elemental abundances are expressed with respect to solar abundances. Normalizations are defined as $(10^{-14}/4\pi d^2) \int n_e n_H dV$, where d is the distance to G352.7–0.1 in cm, n_e and n_p are the electron and hydrogen number densities, respectively (both in cm $^{-3}$) and $V = \int dV$ is the total volume of the emitting region (in cm 3). Fluxes and luminosities are expressed for the energy range from 1.0 to 5.0 keV. Luminosities are calculated assuming a distance of 7.5 kpc to G352.7–0.1. See Section 3.1.

TABLE 5
SUMMARY OF *Chandra* ACIS SPECTRAL ANALYSIS OF G352.7–0.1 (PHABS×VNEI MODEL)

Parameter	Bottom Region	Right Region	Middle Region	Crescent Region	Left Region	Top Region	Whole SNR
N_H (10^{22} cm $^{-2}$)	$3.08^{+0.70}_{-0.60}$	$3.10^{+0.95}_{-0.74}$	$2.68^{+0.76}_{-0.64}$	$2.31^{+1.93}_{-0.91}$	$2.72^{+0.50}_{-0.44}$	$3.24^{+0.72}_{-0.78}$	$2.71^{+0.39}_{-0.33}$
kT (keV)	$0.80^{+0.75}_{-0.25}$	$1.23^{+1.93}_{-0.52}$	$1.24^{+1.30}_{-0.56}$	2.03 (>0.54)	$1.38^{+0.82}_{-0.50}$	$0.68^{+0.82}_{-0.24}$	$1.62^{+0.80}_{-0.46}$
τ (10^{10} cm $^{-3}$ s)	12.7 (>2.00)	$2.74^{+12.0}_{-1.21}$	$1.68^{+1.42}_{-0.62}$	$1.04^{+1.10}_{-0.54}$	$2.46^{+1.34}_{-0.66}$	6.11 (>2.44)	$2.01^{+0.85}_{-0.41}$
Si	$2.4^{+1.1}_{-0.7}$	$2.3^{+2.9}_{-1.2}$	$3.4^{+2.8}_{-1.5}$	4.8 (>1.2)	$2.2^{+1.3}_{-0.8}$	$2.5^{+2.7}_{-0.9}$	$1.9^{+1.3}_{-0.8}$
S	$5.5^{+2.3}_{-1.8}$	$3.8^{+3.6}_{-1.3}$	$8.1^{+2.3}_{-3.7}$	9.8 (>2.0)	$6.6^{+3.4}_{-2.9}$	$6.5^{+6.5}_{-3.5}$	$3.6^{+4.2}_{-1.6}$
Normalization (cm $^{-5}$)	1.2×10^{-3}	6.2×10^{-4}	7.3×10^{-4}	1.8×10^{-4}	8.7×10^{-4}	1.6×10^{-3}	3.6×10^{-3}
χ^2_ν	1.07	1.06	1.04	1.02	1.24	1.25	1.28
χ^2/DOF	70.80/66	63.83/60	78.22/75	70.41/69	104.20/84	76.38/61	266.55/209
Absorbed Flux (ergs cm $^{-2}$ s $^{-1}$)	1.3×10^{-13}	1.2×10^{-13}	1.7×10^{-13}	8.6×10^{-14}	2.4×10^{-13}	1.1×10^{-13}	1.1×10^{-12}
Unabsorbed Flux (ergs cm $^{-2}$ s $^{-1}$)	1.4×10^{-12}	1.1×10^{-12}	1.3×10^{-12}	4.3×10^{-13}	1.7×10^{-12}	1.5×10^{-12}	7.6×10^{-12}
Unabsorbed Luminosity (ergs s $^{-1}$)	9.4×10^{33}	7.4×10^{33}	8.8×10^{33}	2.9×10^{33}	1.1×10^{34}	1.0×10^{34}	5.1×10^{34}

NOTE.—All stated error bounds correspond to 90% confidence intervals. Elemental abundances are expressed with respect to solar abundances. Normalizations are defined as $(10^{-14}/4\pi d^2) \int n_e n_H dV$, where d is the distance to G352.7–0.1 in cm, n_e and n_p are the electron and hydrogen number densities, respectively (both in cm $^{-3}$) and $V = \int dV$ is the total volume of the emitting region (in cm 3). Fluxes and luminosities are expressed for the energy range from 1.0 to 5.0 keV. Luminosities are calculated assuming a distance of 7.5 kpc to G352.7–0.1. See Section 3.2.

TABLE 6

SUMMARY OF *Chandra* ACIS SPECTRAL ANALYSIS OF G352.7–0.1 (PHABS×(VNEI+NEI) MODEL)

Parameter	Left Region	Top Region	Whole SNR
N_H (10^{22} cm $^{-2}$)	$3.75^{+0.49}_{-0.55}$	$4.61^{+0.79}_{-0.77}$	$3.18^{+0.13}_{-0.11}$
kT_{VNEI} (keV)	$1.18^{+0.26}_{-0.20}$	$1.82^{+2.94}_{-0.66}$	$3.24^{+1.40}_{-0.86}$
Si	$2.1^{+0.8}_{-0.6}$	7.0 ± 3.0	$3.4^{+1.2}_{-0.9}$
S	$6.3^{+2.5}_{-1.9}$	17.7 ± 4.9	$9.4^{+3.4}_{-3.0}$
τ_{VNEI} (10^{10} cm $^{-3}$ s)	$2.8^{+1.0}_{-0.6}$	$2.5^{+47.5}_{-0.9}$	1.7 ± 0.3
Normalization $_{VNEI}$ (cm $^{-5}$)	1.42×10^{-3}	1.93×10^{-4}	1.58×10^{-3}
kT_{NEI} (keV)	$0.13^{+0.04}_{-0.02}$	$0.17^{+0.11}_{-0.07}$	$0.24^{+0.08}_{-0.05}$
τ_{NEI} (10^{10} cm $^{-3}$ s)	$7.4^{+23.6}_{-5.0}$	$6.8^{+73.2}_{-5.2}$	$1.4^{+1.1}_{-0.5}$
Normalization $_{NEI}$ (cm $^{-5}$)	6.6	1.7	0.5
χ^2_ν (χ^2/DOF)	1.13 (91.65/81)	1.00 (59.01/59)	1.07 (219.61/206)
Absorbed Flux (ergs cm $^{-2}$ s $^{-1}$)	2.4×10^{-13}	1.2×10^{-13}	1.1×10^{-12}
Unabsorbed Flux (ergs cm $^{-2}$ s $^{-1}$)	7.3×10^{-12}	8.7×10^{-12}	1.4×10^{-11}
Unabsorbed Luminosity (ergs s $^{-1}$)	4.9×10^{34}	5.9×10^{34}	9.4×10^{34}

NOTE.—All stated error bounds correspond to 90% confidence intervals. Elemental abundances are expressed with respect to solar abundances. Normalizations are defined as $(10^{-14}/4\pi d^2 \int n_e n_H dV)$, where d is the distance to G352.7–0.1 in cm, n_e and n_p are the electron and hydrogen number densities, respectively (both in cm $^{-3}$) and $V = \int dV$ is the total volume of the emitting region (in cm 3). Fluxes and luminosities are expressed for the energy range from 1.0 to 5.0 keV. Luminosities are calculated assuming a distance of 7.5 kpc to G352.7–0.1. See Section 3.2.

TABLE 7

SUMMARY OF *Chandra* ACIS SPECTRAL ANALYSIS OF G352.7–0.1 (PHABS×(VNEI+VNEI) MODEL)

Parameter	Left Region	Top Region	Whole SNR
N_H (10^{22} cm $^{-2}$)	$2.59^{+0.14}_{-0.12}$	$4.22^{+0.68}_{-0.60}$	$2.59^{+0.27}_{-0.39}$
kT_{Si} (keV)	$1.78^{+0.32}_{-0.30}$	$0.22^{+0.08}_{-0.06}$	$2.14^{+3.46}_{-0.84}$
Si	6.4 ± 1.5	$2.9^{+11.1}_{-1.7}$	7 (>4)
τ_{Si} (10^{10} cm $^{-3}$ s)	$0.71^{+0.22}_{-0.19}$	$5.8^{+64.2}_{-4.8}$	$0.54^{+0.16}_{-0.13}$
Normalization $_{Si}$ (cm $^{-5}$)	5.08×10^{-4}	0.20	2.57×10^{-3}
kT_S (keV)	$0.61^{+0.07}_{-0.09}$	$0.76^{+0.32}_{-0.28}$	$0.39^{+0.33}_{-0.02}$
S	$13.6^{+11.4}_{-4.1}$	$9.8(>4.0)$	37 (>7)
τ_S (10^{10} cm $^{-3}$ s)	103(>6.8)	950(>1.6)	38 (>2.0)
Normalization $_S$ (cm $^{-5}$)	1.03×10^{-3}	6.92×10^{-4}	9.7×10^{-3}
χ^2_ν (χ^2/DOF)	1.17 (94.48/81)	1.04 (61.26/59)	1.05 (215.69/206)
Absorbed Flux (ergs cm $^{-2}$ s $^{-1}$)	2.4×10^{-13}	1.1×10^{-13}	1.1×10^{-12}
Unabsorbed Flux (ergs cm $^{-2}$ s $^{-1}$)	1.6×10^{-12}	5.0×10^{-12}	7.4×10^{-12}
Unabsorbed Luminosity (ergs s $^{-1}$)	1.1×10^{34}	3.4×10^{34}	5.0×10^{34}

NOTE.—All stated error bounds correspond to 90% confidence intervals. Elemental abundances are expressed with respect to solar abundances. Normalizations are defined as $(10^{-14}/4\pi d^2 \int n_e n_H dV)$, where d is the distance to G352.7–0.1 in cm, n_e and n_p are the electron and hydrogen number densities, respectively (both in cm $^{-3}$) and $V = \int dV$ is the total volume of the emitting region (in cm 3). Fluxes and luminosities are expressed for the energy range from 1.0 to 5.0 keV. Luminosities are calculated assuming a distance of 7.5 kpc to G352.7–0.1. See Section 3.2.

TABLE 8
UNRESOLVED HARD X-RAY SOURCES DETECTED BY *Chandra* TOWARD G352.7−0.1

#	Source	R.A. (J2000.0)	Decl. (J2000.0)	$N_{0.2-10}$	$f_{0.2-2}^{\text{abs}}$	f_{2-10}^{abs}	HR	$L_{\text{abs},2-10}$	Type
1	CXOU J172726.9−350600	17 27 26.97	−35 06 00.2	80	0.1	67.5	1.00	45	mCV?/qHMXB?/AGN?
2	CXOU J172737.7−350616	17 27 37.74	−35 06 16.3	43	0	64.0	1.00	43	mCV?/qHMXB?/AGN?
3	CXOU J172737.9−350724	17 27 37.92	−35 07 24.2	28	0.9	13.3	0.87	8.9	mCV?/AGN?/PSR?/CCO?
4	CXOU J172748.2−350814	17 27 48.22	−35 08 14.4	16	0.1	19.1	0.99	13	mCV?/PSR?
5 ^a	CXOU J172744.0−350719	17 27 44.05	−35 07 18.9	14	0	25.6	1.00	17	K/M-dwarf/AGN?
6 ^b	CXOU J172743.0−350839	17 27 43.03	−35 08 38.8	13	1.1	14.0	0.85	9.4	AGN/PMS-star?

NOTE.—The units of Right Ascension are hours, minutes and seconds while the units of Declination are degrees, arcminutes and arcseconds. $N_{0.2-10}$ is the number of source counts in 0.2–10 keV. The fluxes ($f_{0.2-2}^{\text{abs}}$ and f_{2-10}^{abs} in 0.2–2 and 2–10 keV, respectively) are absorbed (calculated using the *eff2evt* CIAO tool; see <http://cxc.harvard.edu/ciao/threads/eff2evt/>) in units of 10^{-15} ergs cm $^{-2}$ s $^{-1}$. The hardness ratios “HR” are calculated based on the fluxes $f_{0.2-2}^{\text{abs}}$ and f_{2-10}^{abs} , specifically $\text{HR} = (f_{2-10}^{\text{abs}} - f_{0.2-2}^{\text{abs}}) / (f_{2-10}^{\text{abs}} + f_{0.2-2}^{\text{abs}})$. The luminosities $L_{\text{abs},2-10}$ are expressed in units of 10^{31} ergs s $^{-1}$ and are calculated from f_{2-10}^{abs} based on an assumed distance of 7.5 kpc to G352.7−0.1. The abbreviations for type classification are defined as follows: mCV = magnetic cataclysmic variable in low-hard state, qHMXB = quasi-high mass X-ray binary, AGN = active galactic nuclei, PSR = pulsar, CCO = central compact object, PMS-star = pre-main sequence star. See Section 4.4.

^aThis source has a near-infrared counterpart detected with an apparent K-band magnitude of 12.0 and an infrared counterpart detected with an apparent 4.5 μ m magnitude of 11.0.

^bThis source has an infrared counterpart detected with an apparent 4.5 μ m magnitude of 12.7.

TABLE 9
LIST OF KNOWN EJECTA-DOMINATED MIXED-MORPHOLOGY SNRS

SNR	Reference
W44 (G34.7−0.4)	Shelton et al. (2004)
W49B (G43.3−0.2)	Ozawa et al. (2009)
HB 21 (G89.0+4.7)	Lazendic & Slane (2006), Pannuti et al. (2010)
CTB 1 (G116.9+0.2)	Lazendic & Slane (2006), Pannuti et al. (2010)
HB 3 (G132.7+1.3)	Lazendic & Slane (2006)
IC 443 (G189.1+3.0)	Troja et al. (2008), Yamaguchi et al. (2009)
Kes 27 (G327.4+0.4)	Chen et al. (2008)
G344.7−0.1	Yamaguchi et al. (2012)
G352.7−0.1	Kinugasa et al. (1998), Giacani et al. (2009), This paper
G359.1−0.5	Ohnishi et al. (2011)

NOTE.—See Section 4.6.

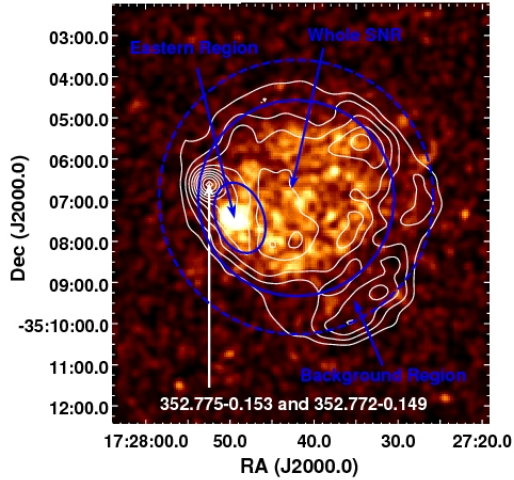


Fig. 1.— *XMM-Newton* MOS1 image (in color) of G352.7–0.1: the image depicts emission from the SNR as detected from the energy range between 0.5 through 10.0 keV. The brightness range of the image is 0 to 0.15 counts s^{−1} arcsec^{−2}. Gaussian smoothing with a radius of 10 arcseconds has been applied. The white contours depict radio emission as detected by the Very Large Array (VLA) at a frequency of 1.4 GHz (Dubner et al. 1993; Giacani et al. 2009): the contour levels range from 0.02 to 0.11 Jy/beam in steps of 0.01 Jy/beam. The location of the background double radio sources WBH 2005 352.775–0.153 and WBH 2005 352.772–0.149 are indicated. The regions of spectral extraction – namely for the bright eastern region, the whole SNR and the background region – are also indicated. Notice that the X-ray morphology is center-filled but the radio morphology is shell-like. These contrasting morphologies are the defining characteristics of MMSNRs. See Section 3.1.

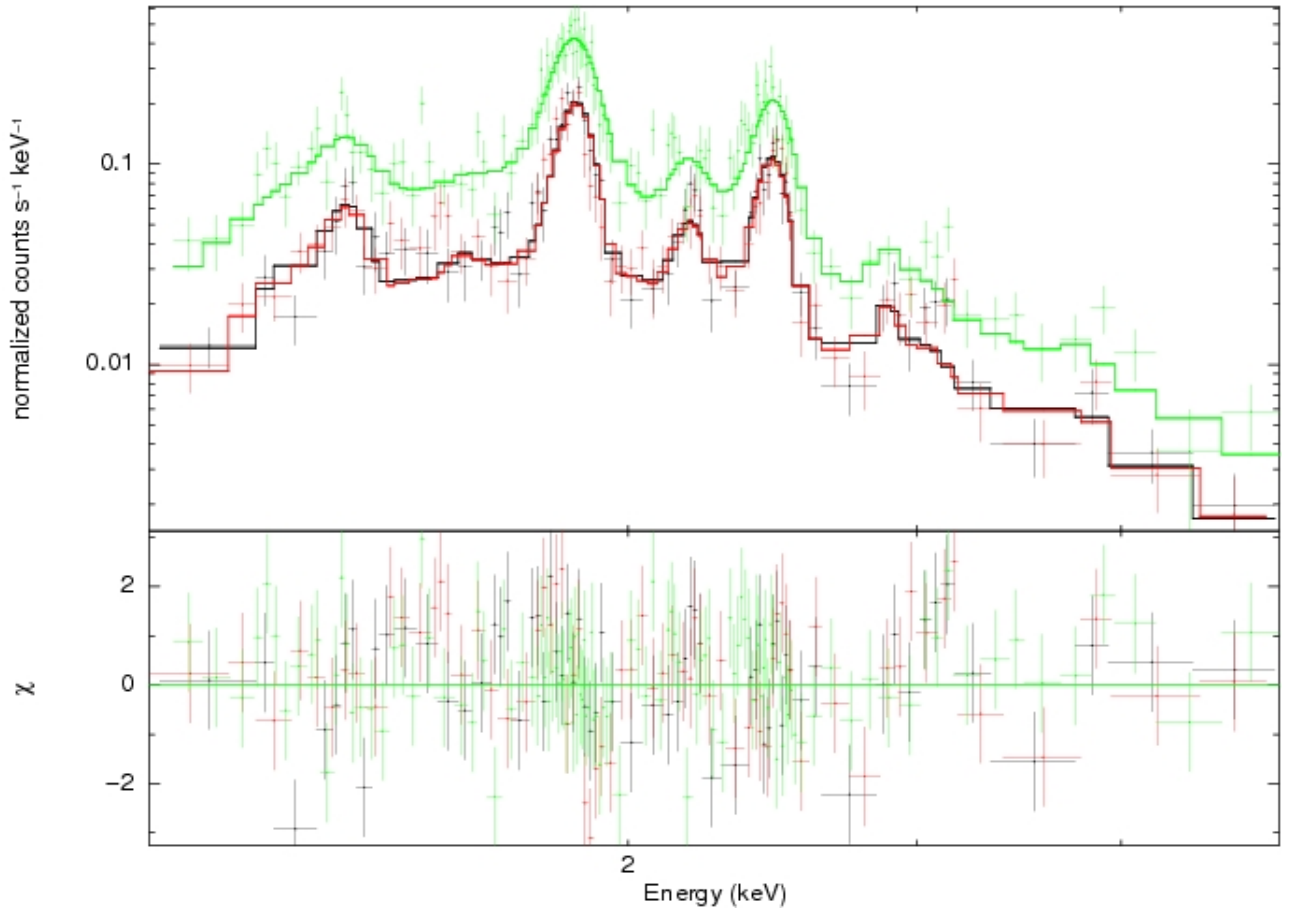


Fig. 2.— Extracted *XMM-Newton* MOS1, MOS2 and PN spectra (in black, red and green, respectively) for the entire diffuse emission of G352.7–0.1 (“whole SNR”) as fitted with a PHABS×VNEI model with variable silicon and sulfur abundances. Notice the prominent silicon and sulfur lines at approximately 1.7 keV and 2.3 keV, respectively. The parameters of the fit to the spectrum are given in Table 4. See Section 3.1.

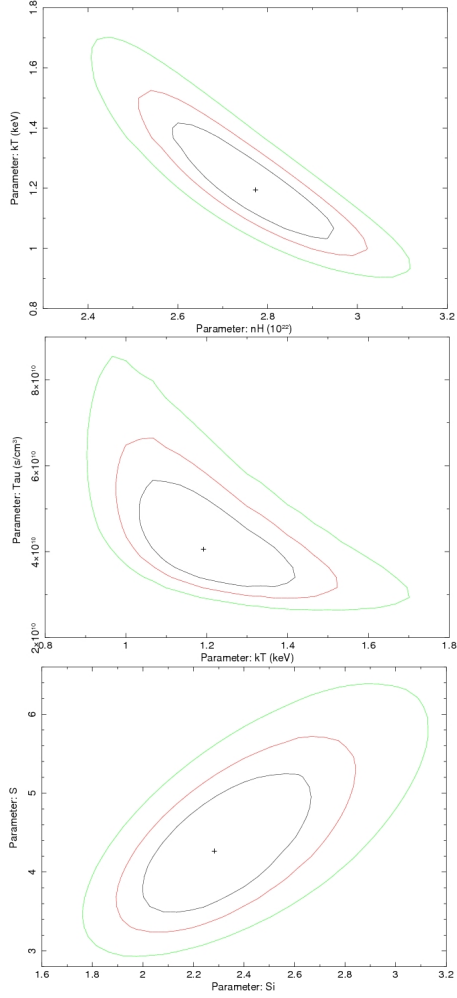


Fig. 3.— Confidence contour plots (N_H vs. kT , kT vs. τ and Si vs. S) for the PHABS \times VNEI fit to the extracted *XMM-Newton* MOS1+MOS2+PN spectra. The confidence contours are at the 1 σ , 2 σ and 3 σ levels. See Table 4 for the fit parameters and Section 3.1 for a discussion of the fit.

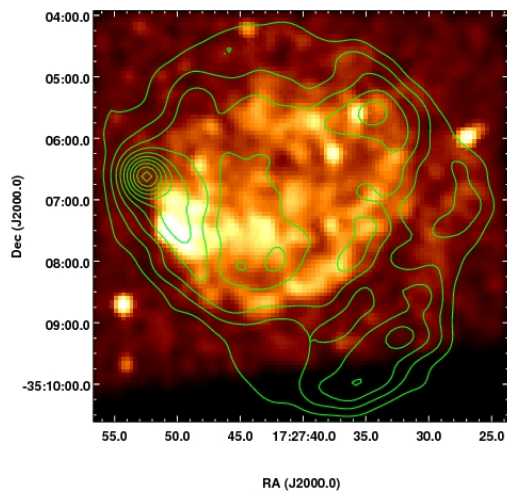


Fig. 4.— Broadband (0.5–7.0 keV) *Chandra* image of G352.7–0.1 as observed with the ACIS-S3 chip: the chip gap can be clearly seen toward the bottom of the figure. The emission has been smoothed with a Gaussian with a radius of 1.5 arcseconds. The green contours depict radio emission as detected by the VLA at a frequency of 1.4 GHz and are placed at the same levels as in Figure 1. See Section 3.2.

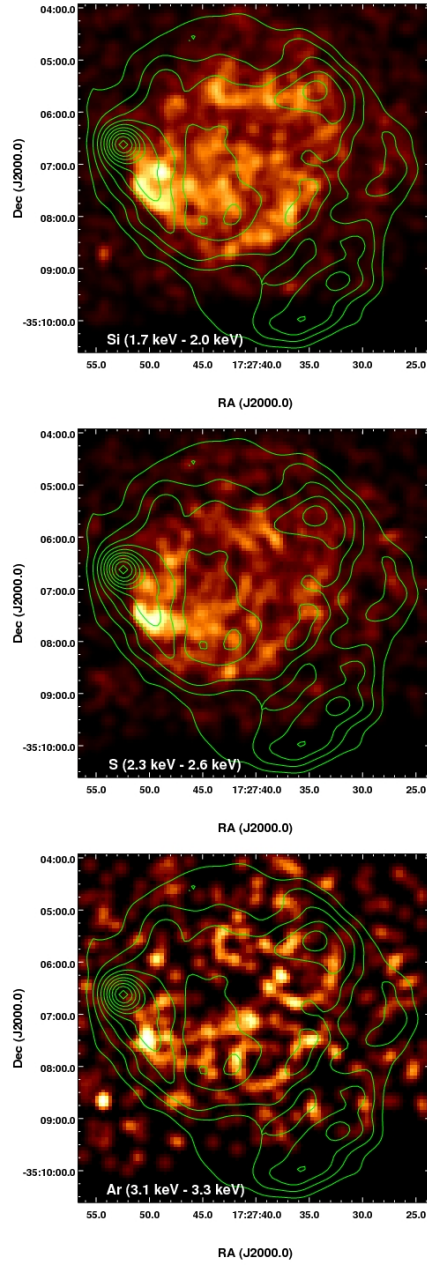


Fig. 5.— Narrowband *Chandra* images of G352.7–0.1 depicting X-ray emission as produced by different elemental species, specifically (from left to right), silicon (1.7 keV - 2.0 keV), sulfur (2.3 keV - 2.6 keV) and argon (3.1 keV - 3.3 keV). In each case, the emission has been smoothed with a Gaussian with a radius of 1.5 arcseconds and green contours depicting radio emission as detected by the VLA at a frequency of 1.4 GHz are overlaid. The radio contours have been placed at the same levels as seen in Figure 1.

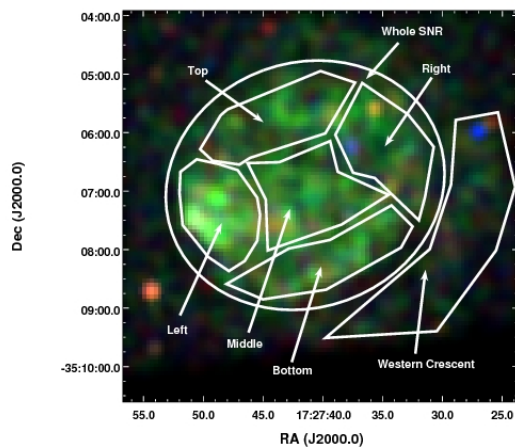


Fig. 6.— Three-color *Chandra* image of G352.7–0.1: the depicted red, green and blue color scales correspond to soft (1.0–1.6 keV), medium (1.6–2.4 keV) and hard (2.4–7.0 keV) emission, respectively. The emission at each energy range has been smoothed with a Gaussian with a radius of 1.5 arcseconds. Regions of extraction of the diffuse emission for spectral analysis are indicated: the corresponding background spectrum is located just to the north of the source and out of the field of view. The entire source and the background region are contained within the field of view of the ACIS-S3 chip. See Section 3.2 and Tables 5, 6 and 7.

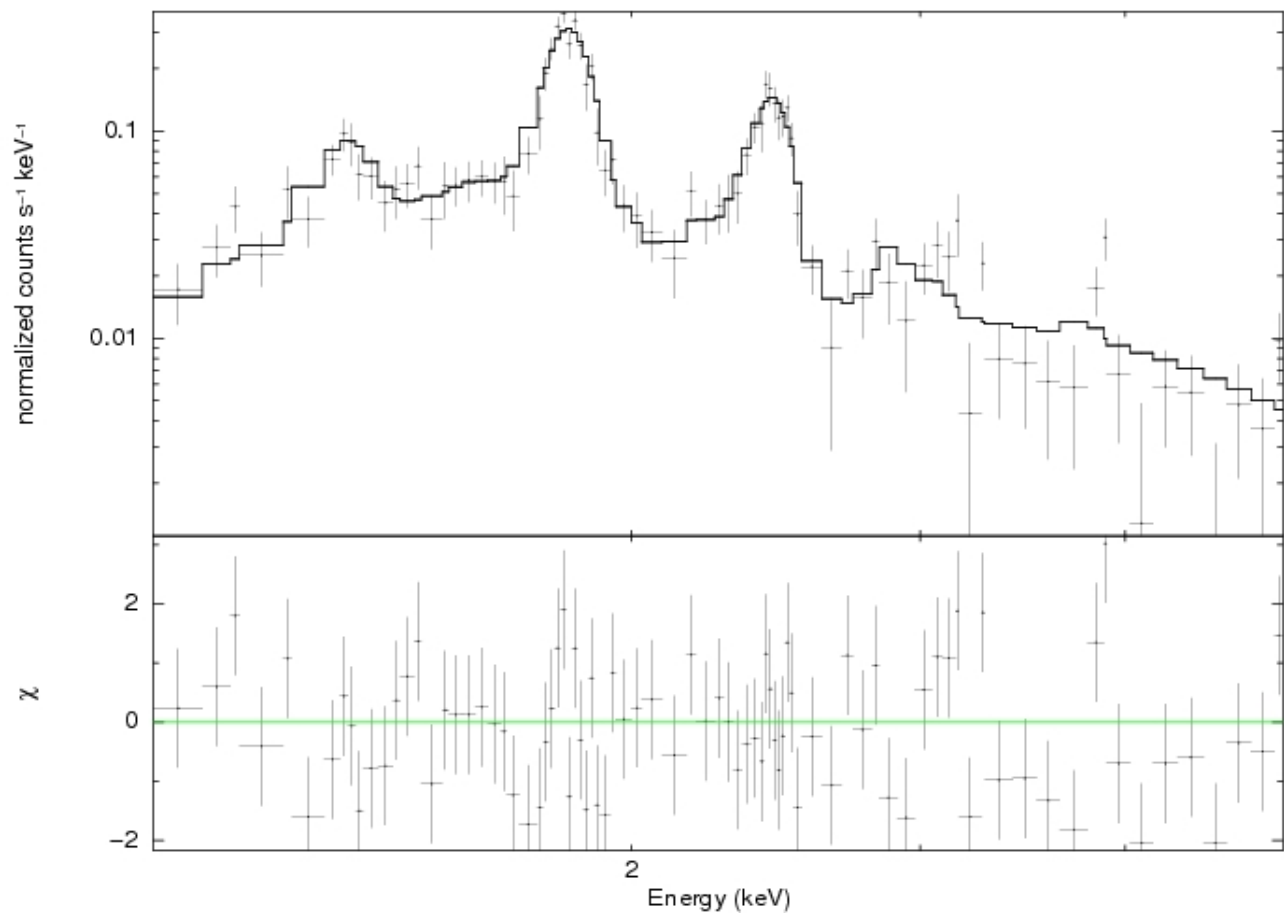


Fig. 7.— Extracted *Chandra* ACIS spectrum of the entire diffuse emission of G352.7–0.1 as fitted with a PHABS×(VNEI+NEI) model. See Section 3.2 and Table 6.

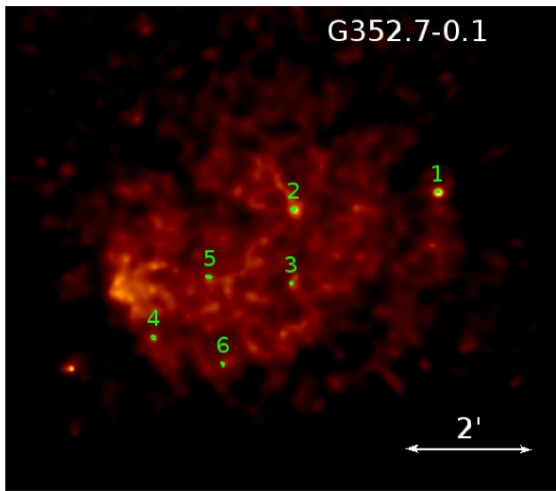


Fig. 8.— A hard-band (2-10 keV) *Chandra* image of G352.7–0.1 with the locations of the point sources detected using `wavdetect` marked and labeled. See Section 4.4 and Table 8.

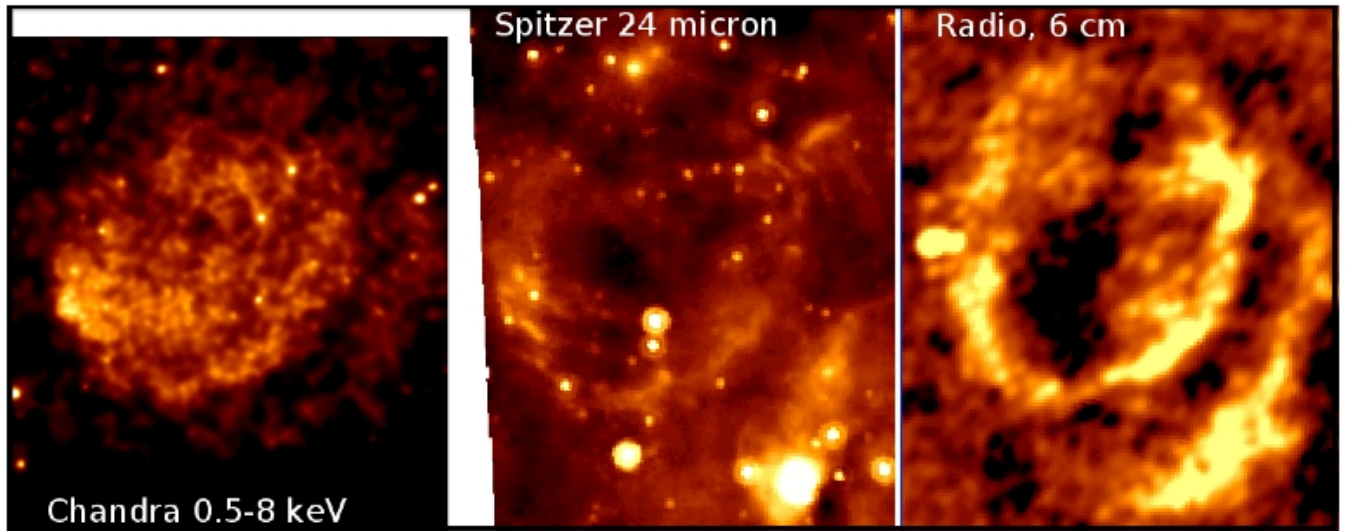


Fig. 9.— Multiwavelength images of G352.7–0.1. (*right*) *Chandra* broadband X-ray image (0.5 - 8.0 keV) smoothed with a Gaussian with a 1.5 arcseconds. (*center*) *Spitzer* MIPS 24 micron image. (*right*) *VLA* 6 cm image. Notice the contrasting X-ray and radio morphologies of the SNR (typical of MMSNRs) and the robust morphological similarities between the infrared and radio images. See Section 4.5.